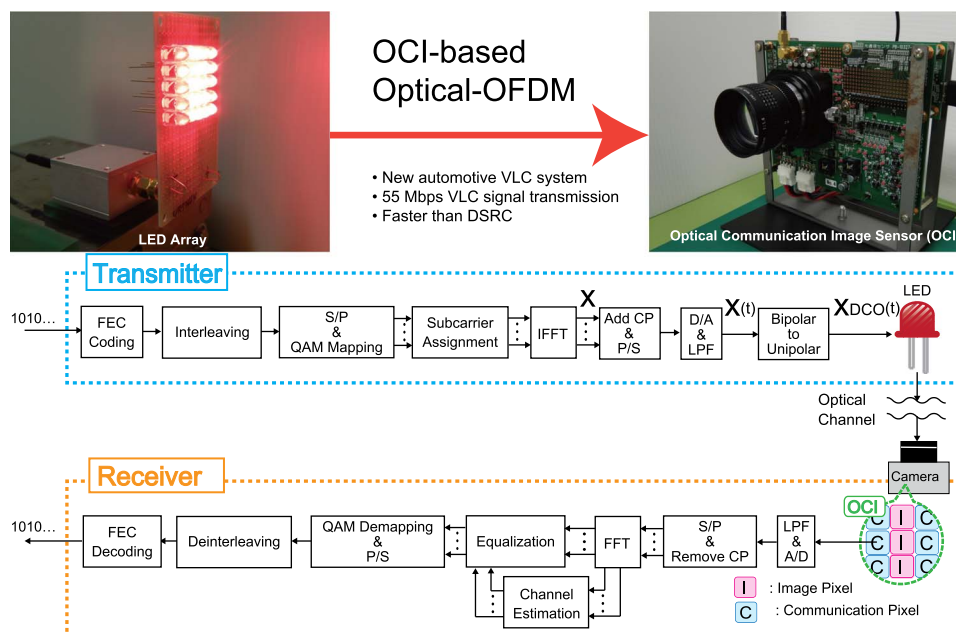# A New Automotive VLC System Using Optical Communication Image Sensor

Yuki Goto, Student Member, IEEE
Isamu Takai, Member, IEEE
Takaya Yamazato, Member, IEEE
Hiraku Okada, Member, IEEE
Toshiaki Fujii, Member, IEEE
Shoji Kawahito, Fellow, IEEE
Shintaro Arai, Member, IEEE
Tomohiro Yendo, Member, IEEE
Koji Kamakura, Member, IEEE

OCI-based Optical-OFDM

• New automotive VLC system
• 55 Mbps VLC signal transmission
• Faster than DSRC

LED Array

Optical Communication Image Sensor (OCI)

A New Automotive VLC System Using Optical Communication Image Sensor

Yuki Goto,[1] *Student Member, IEEE,* **Isamu Takai,**[2] *Member, IEEE,*
Takaya Yamazato,[1] *Member, IEEE,* **Hiraku Okada,**[1] *Member, IEEE,*
Toshiaki Fujii,[1] *Member, IEEE,* **Shoji Kawahito,**[3] *Fellow, IEEE,*
Shintaro Arai,[4] *Member, IEEE,* **Tomohiro Yendo,**[5] *Member, IEEE,* **and**
Koji Kamakura,[6] *Member, IEEE*

[1]Nagoya University, Nagoya 464-8603, Japan
[2]Toyota Central R&D Labs, Inc., Aichi 480-1192, Japan
[3]Shizuoka University, Shizuoka 432-8561, Japan
[4]Okayama University of Science, Okayama 700-0005, Japan
[5]Nagaoka University of Technology, Niigata 940-2188, Japan
[6]Chiba Institute of Technology, Narashino 275-0016, Japan

Abstract: As a new technology for next-generation vehicle-to-everything (V2X) communication, visible-light communication (VLC) using light-emitting diode (LED) transmitters and camera receivers has been energetically studied. Toward the future in which vehicles are connected anytime and anywhere by optical signals, the cutting-edge camera receiver employing a special CMOS image sensor, i.e., the optical communication image sensor (OCI), has been prototyped, and an optical V2V communication system applying this OCI-based camera receiver has already demonstrated 10-Mb/s optical signal transmission between real vehicles during outside driving. In this paper, to reach a transmission performance of 54 Mb/s, which is standardized as the maximum data rate in IEEE 802.11p for V2X communication, a more advanced OCI-based automotive VLC system is described. By introducing optical orthogonal frequency-division multiplexing (optical-OFDM), the new system achieves a more than fivefold higher data rate. Additionally, the frequency response characteristics and circuit noise of the OCI are closely analyzed and taken into account in the signal design. Furthermore, the forward-current limitation of an actual LED is also considered for long operational reliability, i.e., the LED is not operated in overdrive. Bit-error-rate experiments verify a system performance of 45 Mb/s without bit errors and 55 Mb/s with BER $< 10^{-5}$.

Index Terms: Visible light communication (VLC), intelligent transport system (ITS), vehicle-to-vehicle (V2V) communication, infrastructure-to-vehicle (I2V) communication, light-emitting diode (LED), image sensor-based VLC, optical communication image sensor (OCI), optical orthogonal frequency division multiplexing (optical-OFDM).

1. Introduction

Triggered by Google's driverless car, vehicle automation technology has become a hot topic and is being developed worldwide in a rush for an initial launch in the 2020s [1]. Such autonomous
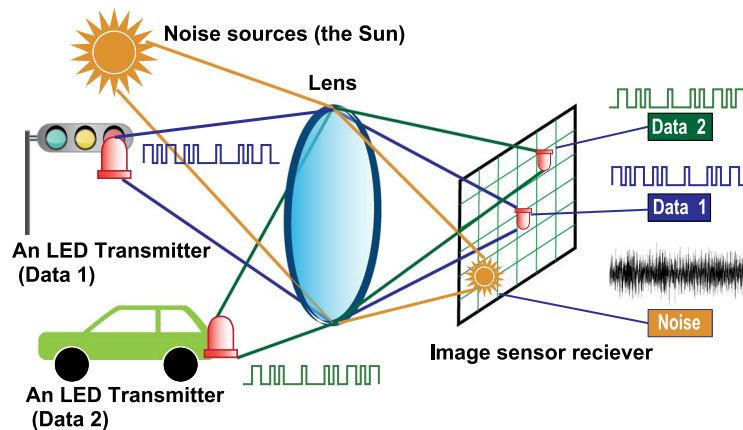
Fig. 1. Spatial separation of multiple sources by an image sensor. The image sensor receiver for the VLC system can discard noise sources such as the Sun and focus only on the pixels that sense desirable sources (i.e., LED transmitters).

vehicles must support autonomous acceleration, steering, and braking. According to the U.S. Department of Transportation (DoT) definition, an autonomous vehicle operates in isolation from other vehicles by using internal sensors [2]. Google's driverless car falls in this category. However, connected or cooperative vehicles exchange sensor information by using vehicle-to-vehicle (V2V) communication and infrastructure-to-vehicle (I2V) communication [3]. Nevertheless, future cars will have the capacity of autonomous and connected vehicles [2].

Vehicle automation systems rely on various advanced sensing devices and systems. Because precision ranging is a key issue for vehicle automation, the ranging performance of mm-wave radar, light detection and ranging (LIDAR) [4], [5], and stereo camera systems, to cite a few examples, are being improved at a rapid rate. Such cameras are used not only for ranging but also for several automotive applications based on image-processing technologies [6], [7]. The significantly high spatial resolution offered by image sensors in these cameras is invaluable for a precise perception of the road environment. The camera, i.e., an image sensor, forms the backbone of the system to implement the major safety applications, such as pedestrian detection and lane detection. It is already becoming an indispensable device; even more image sensors will continuously be installed per a vehicle.

A notable feature of image sensors is that they can receive visible light communication (VLC) signals [8]–[15]. For example, an image sensor can receive data transmitted from LED traffic light, LED signage, LED headlights, LED tail lights, etc. An LED traffic light transmits its signal phase and timing along with additional safety information to cars by blinking its LEDs at a fast rate. LED tail lights and LED headlights, to cite a few examples, can also broadcast internal vehicle information, such as latitude, longitude, and speed, to nearby cars and roadside stations. Since image sensors can detect the position of objects, all these transmission data and their positions are obtained simultaneously. Additionally, image sensors can spatially separate objects, as shown in Fig. 1. This ability enables the receiver to discard noise sources, such as the Sun, streetlights, and other lighting sources, and focus only on the pixels to which the LED light strikes. Therefore, a high signal-to-noise ratio (SNR) can be achieved even in outdoor environments [9]. Moreover, the communication performance of VLC systems based on image sensor receivers remains stable as communication distance increases [9]. The incident light power per a pixel remains unchanged as long as the projected image of the LED transmitter occupies several pixels. Thus, the SNR is independent of distance. From above, image-sensor-based VLC systems offer unique features: position detection of the LED transmitter, high SNR due to the ability of spatial separation, and stable performance as communication distance increases.

To an image sensor receiver, automotive VLC applications give severe hurdles that must be overcome: achieving a high data rate, high dynamic range, and accurate and fast LED
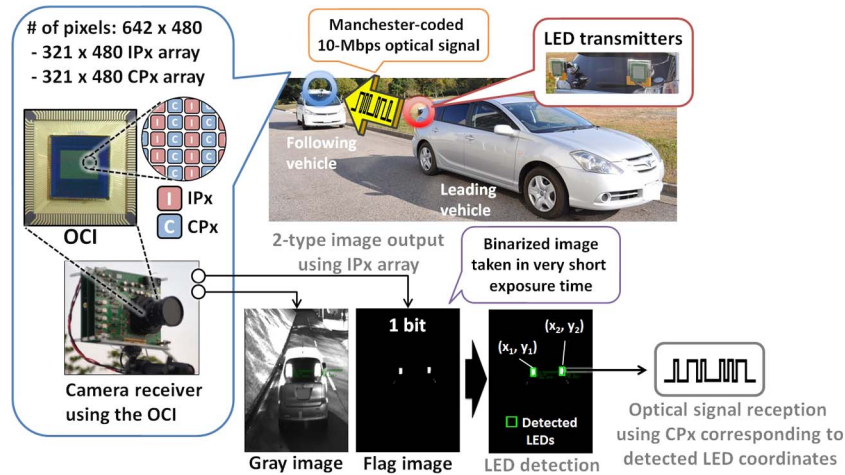
Fig. 2. Entire operation of OCI-based V2V system. The OCI outputs a conventional gray image and a 1-bit flag image. Based on the flag image, the LED regions are detected and, then, CPx corresponding to the coordinates of the LED receives optical signals.

detection. To receive the various internal vehicle data and large-size multimedia data (e.g., image and video data), the receiver must offer Mbps-class optical-signal reception performance. Furthermore, because outdoor lighting is uncontrolled and has a high intensity, a high dynamic range is required of photodetectors (i.e., pixels) in the receiver to prevent signal outputs from being saturated by strong lights. Moreover, the receiver must find quickly and correctly LED transmitters in complicated scene images at a low computational cost. In previous technologies, including nonautomotive VLCs [10], [11], [13], [15], there are two types of receivers using high-speed (high-frame-rate) image sensors and special image sensors that is developed for optical wireless communications. However, none of these earlier receivers fulfill all the requirements mentioned above.

To realize an automotive VLC system, we have already developed an optical communication image sensor (OCI) [16] that satisfies all requirements, and it is fabricated with existing 0.18-μm CMOS (complementary metal-oxide semiconductor) technology to keep costs low. The remarkable feature of this OCI is that its pixel array is composed of two types of pixels: communication pixels (CPx) for receiving high-speed optical signals and image pixels (IPx) for obtaining scene images. With a logarithmic response, CPxs provide a substantially improved response to light-intensity variations, so our optical V2V system using the OCI has achieved 10-Mbps Manchester-coded optical-signal reception in an outdoor environment without signal saturation [17]. Moreover, the OCI has an output function of "1-bit flag image" which only reacts to high-light-intensity objects, such as LEDs [16]. The flag image, in which no unnecessary objects exist, facilitates quick and accurate LED detection, and the optical V2V system has successfully demonstrated real-time LED detection in outdoor driving [17]. Note that the "1-bit flag" detection method uses no feature of the modulated signal [16].

Fig. 2 shows the entire operation of the OCI-based V2V system we developed [17]. First, the OCI outputs a conventional gray image and the 1-bit flag image. Based on the flag image, the LED regions are detected and the CPx corresponding to the central coordinates of the LED regions is selected. Finally, the optical signal received by the selected CPx is outputted from the camera receiver. This operation is repeated continuously, and therefore, both high-speed optical-signal reception and satisfactory LED-transmitter detection are achieved. We expect that the OCI will pave the way for the development of automotive VLC systems.

In this paper, we propose a more advanced automotive VLC system based on the OCI. We adopt optical orthogonal frequency division multiplexing (optical-OFDM) and achieve 55 Mbps VLC signal transmission. The frequency-response characteristics and circuit noise of the OCI are taken into account in the design of the optical-OFDM. Furthermore, the forward-current
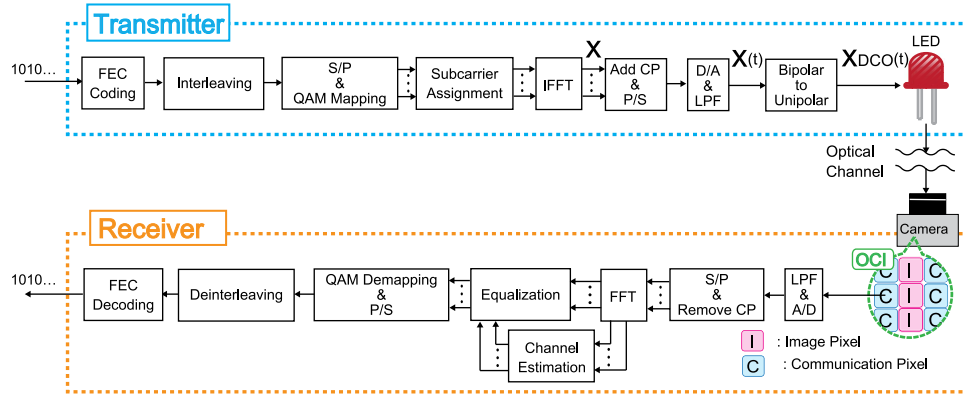
Fig. 3. General system model of OCI-based optical-OFDM.

limitation of an actual LED is also considered for practical industrial production; that is, in terms of long-term reliability. For example, the maximum instantaneous current is restricted by the maximum rating of the pulse-forwarding current given on the manufacture's data sheet according to [18]. Moreover, the average forward current is set to the rated current to account for the primary role of LEDs as a lighting source.

Note that data rate of 55 Mbps is faster than the currently available rate for V2V and I2V communication systems, known as dedicated short-range communication (DSRC). For example, in Europe, the DSRC standard uses a 10 MHz bandwidth at 5.795–5.805 GHz and achieves 500 kbps (downlink) and 250 kbps (uplink) [19]. In Japan, the DSRC standard is called ARIB STD-T75, uses a 5 MHz bandwidth at 5.770–5.850 GHz, and achieves 4 Mbps [19], [20]. The new 700 MHz band communication standard for ITS is also standardized by ARIB STD-T109 and its maximum data rate is 18 Mbps with a 10 MHz bandwidth [21]. DSRC is based on the IEEE 802.11p standard, and its maximum data rate is 27 Mbps with a 10 MHz bandwidth, and it optionally supports 54 Mbps with a 20 MHz bandwidth [19], [22]. Thus, the communication performance of the OCI-based VLC system is equivalent to the DSRC standards.

This paper is organized as follows: The OCI-based optical-OFDM system is detailed in Section 2. Section 3 presents a selection of optical-OFDM signal processing parameters. Section 4 provides experimental results and discussion, and Section 5 concludes.

2. OCI-Based Optical-OFDM System Model

Optical-OFDM is a promising modulation scheme for achieving high-data-rate VLC systems [23], [24]. In conventional OFDM, which is commonly used in wireless radio systems, the transmission signals are bipolar and complex. However, optical signals must be real and non-negative. Therefore, conventional OFDM is modified to optical-OFDM to generate real, non-negative signals.

Fig. 3 shows a general system model of an OCI-based optical-OFDM. The information bits are first encoded by forward error correction (FEC) techniques such as convolution code. Encoded information bits are then interleaved and converted from serial to parallel (S/P). A block of complex symbols are drawn from multilevel quadrature amplitude modulation (M-QAM) and assigned to each subcarrier component, resulting in a block of data symbols denoted by $\mathbf{X} = [X_0, X_1, X_2, \ldots, X_{N-2}, X_{N-1}]$, where N is the number of subcarriers, and $\mathbf{X}$ satisfies

$$X_m = X_{N-m}^* \quad \text{for} \quad 0 < m < \frac{N}{2} \tag{1}$$

where the asterisk denotes complex conjugation, and the DC components X_0 and $X_{N/2}$ are set to zero (i.e., $X_0 = X_{N/2} = 0$). Note that the number of unique data-carrying subcarriers is $(N/2) - 1$. Because of the structure of $\mathbf{X}$, the output signal x of the inverse fast Fourier

transform (IFFT) is real and not complex. The real signal is added by cyclic prefix (CP) and converted from parallel to serial (P/S). Following digital to analog (D/A) conversion and low-pass filtering, the resulting time-domain signal $x(t)$ is used to modulate the intensity of a LED. However, the bipolar signal $x(t)$ must be converted to unipolar. Based on the bipolar-unipolar conversion process, several optical-OFDM schemes have been reported [25], [26]. In the present work, we use the major optical-OFDM scheme of DC-biased optical-OFDM (DCO-OFDM).

2.1. DCO-OFDM

In the DCO-OFDM scheme, the unipolar time-domain signal is converted from bipolar signal by a DC bias. The kth time-domain sample of x, x_k is given by

$$x_k = \frac{1}{N} \sum_{m=0}^{N-1} X_m \exp\left(\frac{j2\pi km}{N}\right) \tag{2}$$

where X_m is the mth subcarrier component of **X**. Signal x is then P/S and D/A converted, resulting in $x(t)$, which, for a large number of subcarriers, can be modeled as a Gaussian random variable with a zero mean and variance $\sigma^2 = E\{x(t)^2\}$. Next, a suitable DC bias is added to $x(t)$ and any remaining negative components are clipped at zero to generate a unipolar signal. Because OFDM signals have a high peak-to-average power ratio (PAPR), a large bias is required to eliminate negative components completely; however, a large bias leads to a significant degradation of the optical power efficiency. Therefore, a moderate bias is normally used and the remaining negative components are clipped, resulting in clipping noise [26]. B_{DC} denotes the DC bias level and is set relative to the standard deviation of $x(t)$

$$B_{DC} = \mu \sqrt{E\left\{x(t)^2\right\}} \tag{3}$$

where μ is a proportionality constant. Any negative component that remains after the addition of B_{DC} is clipped at zero. In addition, upper peaks at $2B_{DC}$ are also clipped to eliminate overly large signal components, resulting in the signal $x_{DCO}(t)$. In other words, $x_{DCO}(t)$ satisfies

$$0 \leq x_{DCO}(t) \leq 2B_{DC}. \tag{4}$$

Next, $x_{DCO}(t)$ is inputted into an optical modulator and transmitted as an optical signal.

At the receiver, a received optical signal is first converted to an electrical signal by using the photodiode in the selected communication pixel of the OCI. Processing after this point is the same as for a conventional OFDM receiver. Following S/P conversion, the FFT output signal is equalized in the frequency domain. Channel-equalizing factors are obtained by averaging the training symbols for each subcarrier that are transmitted prior to the data-carrying symbols. The equalized symbols are demodulated and de-interleaved. Finally, the received bits are decoded by the Viterbi soft-decision algorithm (the transmitter is assumed to be equipped with a convolutional encoder).

Note that DCO-OFDM signal processing involves several parameters, such as the modulation scheme of each subcarrier, the proportionality constant μ, the amplitude of the transmission signal $x_{DCO}(t)$, and the signal bandwidth. During signal design, it is important to consider the actual characteristics of the reception device being used (i.e., the OCI). In the following sections, the actual frequency response and internal noise characteristics of the OCI receiver are described.

2.2. Frequency-Response Characteristics of OCI

Fig. 4 shows the results of frequency-response measurements of the CPx. The vertical axis corresponds to the frequency response in dB, according to responses to a 100 kHz component.
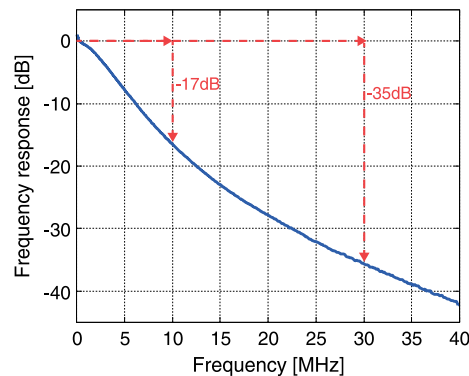
Fig. 4. Measured frequency response of the CPx. The CPx has a high dynamic range by the logarithmic response structure to be used in outdoor lighting environments. By this response characteristic, the frequency response of the OCI is not flat, but it continuously decreases as the frequency increases [16].
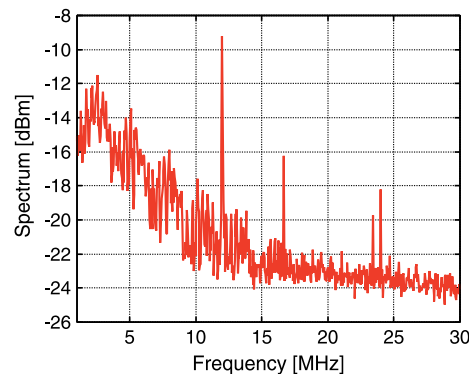
Fig. 5. Measured noise spectrum of a CPx output. The large narrowband noise at 12 MHz, and the low-frequency noise component (several MHz) are shown. These noises arise from circuits to obtain the gray and flag images; then, they obscure received signals.

The desirable frequency response is, of course, flat. However, the CPx suffers from loss in signals with high-frequency components since the CPx has employed the logarithmic response structure to enlarge the dynamic range.

Results show that the frequency response continuously declines as the frequency increases. If the signal bandwidth is 10 MHz, the loss in higher frequency components reaches −17 dB; if the signal bandwidth is 30 MHz, the loss in higher frequency components reaches −35 dB. From these results, increasing signal bandwidth to achieve higher data rates would be difficult, and therefore, appropriate selection of the bandwidth is important to obtain the desired communication performance.

2.3. Circuit-Noise Characteristics

In addition to the high-frequency-attenuation characteristics, the noise generated from the OCI circuits also affects the communication performance. Because the image-sensor-based VLC system has a capacity for spatial separation of multiple sources, ambient and reflected lights are not dominant noise sources relative to circuit noise. In particular, the circuit noise has a specific property that is due to the OCI structure.

Fig. 5 shows the noise spectrum measured for an OCI receiver. This noise spectrum is from the received signal output and is analyzed when the LED-detection function of the OCI receiver

is active. Fig. 5 reveals a particularly large narrowband noise at 12 MHz, which arises because the image-obtaining circuits for LED detection are being located around the pixel arrays of the OCI. The clock frequency of the circuits is 12 MHz, and the clock pulses propagate to the received signal. Thus, this noise is unavoidable if the image-obtaining circuits are active for LED detection. Furthermore, Fig. 5 also shows a relatively large noise in the low-frequency region (several MHz). Besides the frequency response, these noise characteristics lead to the different SNRs for each subcarrier in a multicarrier modulated signal (i.e., optical-OFDM signals).

3. Optimization of Signal-Processing Parameters Considering Characteristics of LEDs and OCI

To achieve higher data rates, we must consider the channel characteristics when setting the parameters for a signal-processing scheme, i.e., the characteristics of the LED transmitter and the OCI receiver. In this section we thus first determine the forward-voltage range of the LED transmitter by considering the practical limitations specified by the LED data sheet. Second, we select the proportionality constant μ and signal bandwidth based on the channel capacity calculated from the estimated SNR of each subcarrier. Finally, we apply simple bit loading for the DCO-OFDM. Bit loading allocates data so that the throughput of each subcarrier is maximized and matches the channel characteristics. In the OCI-based DCO-OFDM system, the high-frequency attenuation and non-white circuit noise limit the available bandwidth and the different SNRs of each subcarrier. Thus, the adaptation of bit loading is expected to provide effective data transmission and improve performance.

3.1. Forward-Current Limitation Based on Actual LED

In the transmission of the above-mentioned DCO-OFDM signal $x_{\text{DCO}}(t)$, the range of forward current through the LED transmitter is directly linked to the radiated optical-signal amplitude. Therefore, the current range should be set as large as possible to ensure a high SNR.

However, the forward current has several limitations from a practical point of view. First, the maximum instantaneous current is necessarily restricted as per the specifications of the LED to ensure that the LED chip does not overheat. The current value is generally defined as the absolute maximum rating of the pulse-forwarding current given on the manufacturer's data sheet. Second, since each LED has a minimum threshold known as the turn-on voltage (TOV), which corresponds to the onset of current flow and light emission, the minimum forward voltage is also determined automatically. Finally, the average forward current of the LED, which is DC, should be set to the rated current because a primary role of the LED is as a light source in the automotive field. Note that these conditions about forward current correspond to the forward voltage through the LED, such as minimum, average, and maximum forward voltage.

In the work, a red LED (UR5366X, Stanley Electric Co. Ltd.) is used as an optical transmitter. According to the specifications, the absolute maximum rating of the pulse-forwarding current is 100 mA, and the rated current is 20 mA. Additionally, Fig. 6 shows the relationship measured between the forward voltage V_F through the LED and the forward current I_F. Fig. 6 shows that the TOV is about 1.72 V, the voltage corresponding to 20 mA is about 2.08 V, and the voltage corresponding to 100 mA is about 2.7 V. Thus, the amplitude of $x_{\text{DCO}}(t)$ complies with the practical limitations defined as follows: first, the average voltage is set to correspond to the rated current, 2.08 V; second, any minimum or maximum peaks of the signal must not exceed the TOV and the maximum allowed voltages of 1.72 V and 2.7 V, respectively.

As mentioned above, maximizing the amplitude of the $x_{\text{DCO}}(t)$ under these conditions is desirable for high SNR. Because the mean of $x_{\text{DCO}}(t)$ equals the added DC-bias level and the waveform is symmetrically clipped, the peak-to-peak voltage V_{p-p} of $x_{\text{DCO}}(t)$ is $2(2.08 - 1.72) = 0.72$ V, as shown in Fig. 6. Although the LED can tolerate the higher voltage, V_{p-p} is determined by the TOV for the V–I characteristic of this LED.

Fig. 6 shows some nonlinearity in the low-forward-voltage region, near the TOV. The signal $x_{\text{DCO}}(t)$ can be modeled as a Gaussian random variable, in which case, its major components
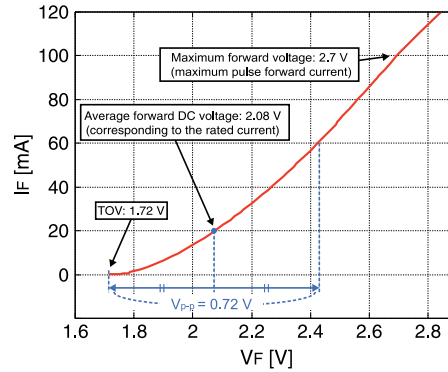
Fig. 6. Measured relationship between forward voltage V_F and forward current I_F of the UR5366X LED. From the specifications, the absolute maximum rating of the pulse forwarding current is 100 mA, and the rated current is 20 mA. The voltages corresponding to the currents of 100 and 20 mA are 2.08 and 2.7 V, respectively, and the turn-on voltage is 1.72 V. According to these voltages, the signal amplitude is set to 0.72 V_{p-p}.

concentrate the voltage near the DC bias point of 2.08 V. Thus, although the nonlinearity of the LED would lead to performance degradation, the effect is not significant.

We, however, note that LED nonlinearity would have significant impact on the performance of DCO-OFDM, especially for high modulation orders [27]. Also, the OFDM generally suffers from high PAPR. As discussed in Section 2.1, the selection of the DC bias level μ is the key parameter to reduce the effect of LED nonlinearity and PAPR while the adaptation of a high order modulation depends on the channel capacity. In the following subsection, we discuss the selection of the DC bias level μ and the channel capacity of our DCO-OFDM considering the signal bandwidth of the OCI, as described in Section 2.2.

3.2. Selection of μ and Signal Bandwidth Based on Channel Capacity

We investigate the two parameters for DCO-OFDM signal processing that are based on the channel capacity: μ and signal bandwidth. In this work, we calculated the channel capacity by estimating the measured SNR from the concept of error vector magnitude (EVM) [28], which is a measure of errors between the ideal symbols and measured symbols normalized by the magnitude of the ideal symbol.

If the normalized ideal and measured symbols are denoted by S_i and S_m, respectively, then the estimated SNR is given by

$$\mathrm{SNR}_{est} = \frac{\|s_i\|^2}{\|e\|^2} = \frac{\|s_i\|^2}{\|s_m - s_i\|^2} \tag{5}$$

where e is the error. In general, the EVM is defined as the average value of the results for a number of symbols. The total channel capacity C is given by

$$C = \sum_{k=1}^{N} C_k = \sum_{k=1}^{N} B_k \log_2(1 + \mathrm{SNR}_k) \qquad [\mathrm{bps}] \tag{6}$$

where N is the number of subcarriers and C_k is the channel capacity of a certain subcarrier. We average SNR_{est} from 1000 symbols for each subcarrier and then calculate C_k and C. Notice that the communication performance, or, equivalently, the received SNR, of the OCI-based VLC system is stable against communication distance, as long as the image sensor can resolve the light source to within a few pixels [9].

Additionally, the image sensor receiver can discard noise sources by applying its spatial-separation ability. Therefore, the estimated and averaged SNRs from the EVM are almost

TABLE 1

Calculated C [Mb/s] for μ and signal bandwidth

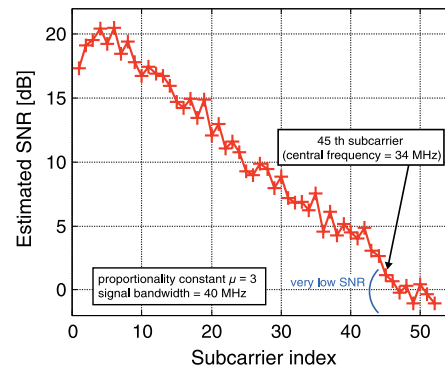|		Signal bandwidth [MHz]					
		12.8	16	20	26	32	40
μ	2.5	63.7	79.3	98.5	120.5	138.5	142.8
	2.75	65.3	81.5	97.6	120.0	140.8	143.0
	3	67.2	82.7	99.6	124.6	141.5	142.4
	3.25	67.6	83.1	101.4	123.9	138.8	137.8
	3.75	68.9	83.5	103.1	119.7	131.4	134.4

Fig. 7. Estimated SNR of each subcarrier. The parameter $\mu = 3$, and the signal bandwidth is 40 MHz. The SNRs of high-frequency subcarriers, particularly subcarriers 45–52, are low, and it would be impractical to modulate the high-frequency subcarriers. The central frequency of subcarrier 45 is 34 MHz.

constant and signal-processing parameters can be optimized based on the SNR in practical mobile environments.

To compare channel capacities with the different parameters, we conducted preliminary experiments to estimate the SNR of each subcarrier for multiple values of μ and the signal bandwidth.

Note that the transmission power is allocated so that all subcarriers have the same power in the experiments, which guarantees the Gaussian-approximation capability for the signal $x_{\text{DCO}}(t)$ and a uniform effect of signal clipping on each subcarrier. Additionally, the signal amplitudes are set to 0.72 V_{p-p} as per the previous discussion.

Table 1 shows the results of the measured channel capacity C for multilevel proportionality constant μ and signal bandwidth. Note that C is in units of Mbps. In the measurements, the number of subcarriers is fixed and set at 52. Therefore, the subcarrier interval, or equivalently the bandwidth of each subcarrier, increases in proportion to the signal bandwidth.

The signal bandwidths are set to several values ranging from 12.8 to 40 MHz. When the bandwidth is 12.8 MHz, the component of the highest-frequency subcarrier is attenuated by about 20 dB, as shown in Fig. 4. If the bandwidth is 40 MHz, the attenuation of the component exceeds 40 dB. Table 1 shows that the capacities differ drastically for different signal bandwidths and basically increase with increasing signal bandwidths. However, almost no differences exist between a signal bandwidth of 32 MHz and that of 40 MHz, which implies that high-frequency subcarriers whose central frequency exceeds 32 MHz contribute little to the total capacity. For instance, the estimated SNR of each subcarrier with $\mu = 3$ and signal bandwidth = 40 MHz is shown in Fig. 7. The SNR of high-frequency subcarriers, especially subcarriers 45–52, are low,

and modulating the high-frequency subcarriers would be impractical. The central frequency of subcarrier 45 is 34 MHz. Thus, the practical signal bandwidth should be around 30 MHz or at most 34 MHz. Thus, 32 MHz is the most appropriate value within the measured bandwidths and is therefore used in following experiments.

Additionally, μ is set to 2.5, 2.75, 3, 3.25, and 3.5 in the experiments. If μ is too small, the effect of clipping the waveform is significant and degrades the capacity. In contrast, an excessively large μ leads to optical signals with a lower amplitude compared with V_{p-p} and degrades the SNR of each subcarrier or, equivalently, the total capacity. The appropriate value must be selected. Although the optimal DC-bias of DCO-OFDM that corresponds to μ is already mentioned in [25], it has not been sufficiently studied for the case in which the modulation schemes differ for each subcarrier and in which the LED has nonlinear I-V characteristics. From Table 1, for a signal bandwidth of 32 MHz, $\mu = 3$ is the best choice and is thus used in the following experiments.

3.3. Applying Simple Bit Loading for DCO-OFDM

When the subcarriers of the DCO-OFDM signal are modulated by M-QAM, the constellation order M can differ from that of the other subcarriers. According to the bit-loading technique, data bits corresponding to the constellation order M can be adaptively allocated to each subcarrier based on their SNR to suit the channel characteristics.

In this work, we apply the very simple bit-loading algorithm [29]. The purpose of the algorithm is to allocate bits into the subcarriers to minimize the average bit error rate (BER) and thereby guarantee the target bit rate or, equivalently, the target number of bits per OFDM symbol. Many reported bit-loading algorithms optimize not only bit assignment to subcarriers but also power allocation. However, power allocation for each subcarrier is fixed in this work because, if allocated power varies significantly for each subcarrier, the discussion above of selecting appropriate values of μ and the signal bandwidth would have no meaning. Thus, in this work, for the sake of simplicity, we only optimize bit assignment to subcarriers.

In the adopted algorithm, the number of bits per symbol of each subcarrier is assumed to range from 1 to 8, such as binary phase-shift keying 4-QAM, 8-QAM, 16-QAM,. . ., and 256-QAM. Additionally, the BERs of BPSK and M-QAM in AWGN channel for a certain SNR can be calculated from the closed-form expression given in [30] and [31].

The outline of the algorithm is as follows: First, the largest constellation order within the assumed modulation schemes, in this case 256-QAM, is applied as an initial set for each subcarrier. Second, an average BER is calculated for the case in which the number of assigned bits for a certain selected subcarrier is reduced by 1 bit. For example, the constellation order of the first subcarrier is reduced to 128-QAM, and those of the other subcarriers remain in 256-QAM and the average BER is calculated. The BER is calculated for all subcarriers (i.e., the case in which the second subcarrier is modulated by 128-QAM, and the other subcarriers are modulated by 256-QAM, and so on), and then, the subcarrier corresponding to the smallest average BER in the former calculation is determined. Next, the number of assigned bits for the chosen subcarrier is reduced by 1 bit and the bit assignment is updated. The average BER is calculated, the bits assigned to the subcarriers are reduced, and this process is repeated as long as the bitrate corresponding to the updated bit assignment exceeds the target bitrate.

Note that, if the target throughput is 50 Mbps and convolutional coding with rate 1/2 is applied, the target bit rate of the bit-loading algorithm should be set to 100 Mbps. Equivalently, considering the code rate, the target number of bits per OFDM symbol should be doubled. Additionally, In OFDM systems we must consider the degradation of the transmission efficiency because of the added training symbols and CP.

Fig. 8 shows the estimated SNR of each subcarrier with $\mu = 3$ and a signal bandwidth of 32 MHz. In addition to the effect of high-frequency attenuation of the OCI, the effect of the internal noise of the OCI is also shown in Fig. 8. For example, the SNRs of low-frequency subcarriers (i.e., subcarriers 1–3) are less than that of the subcarrier 5 because of the low-frequency-noise
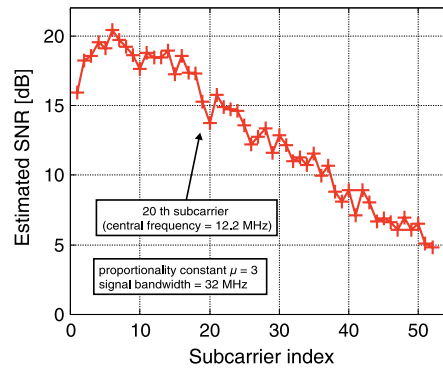
Fig. 8. Estimated SNR of each subcarrier with $\mu = 3$ and a signal bandwidth of 32 MHz.
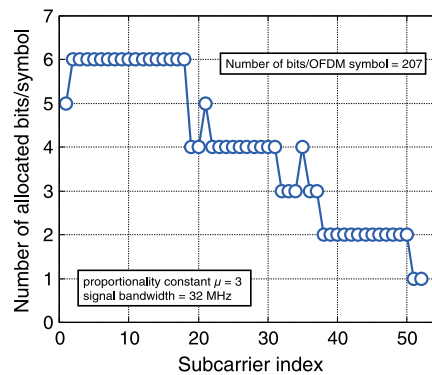

Fig. 9. Number of allocated bits per symbol for each subcarrier when the target number of bits per OFDM symbol is 207.

component from the OCI internal circuits. The SNR of the subcarrier 20 with a central frequency of 12.2 MHz is also slightly less than that of the adjacent subcarriers because of the effect of the large narrowband noise at 12 MHz.

As an example of bit loading, Fig. 9 shows the number of allocated bits per symbol of each subcarrier when the target number of bits/OFDM symbol is set to 207. The allocated bits per symbol for subcarriers range from 1 to 6. Note that the bits allocated to a certain subcarrier that has a very low SNR could be zero when the target number of bits per OFDM symbol is small. In this case, the subcarrier should not be allocated any bits, and therefore, the effective signal bandwidth decreases. Note that once the bit loading is determined, we fix the allocated bits per symbol of each subcarrier.

4. Experimental Results

4.1. System Setup for Optical-OFDM Using OCI

To evaluate the performance of OCI-based optical-OFDM system discussed in the previous section, we conducted data-transmission experiments.

Fig. 10 shows a LED transmitter and the camera receiver containing the OCI. The experimental setup (a LED transmitter and a camera receiver containing the OCI) is shown in Fig. 11. Signal $x_{\mathrm{DCO}}(t)$ modulates the LED and is transmitted through free space by optical signals. The distance between the transmitter and receiver is 1.5 m, and these are fixed in space. Although the experiments are conducted in the fixed conditions, the LED detection circuits of the OCI are
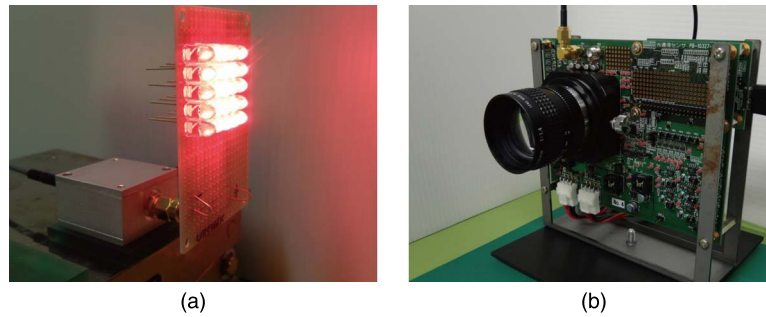
(a)   (b)

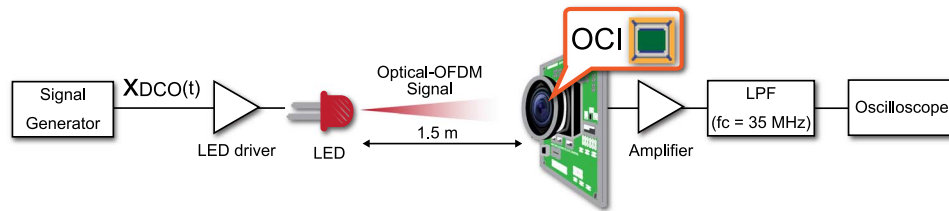Fig. 10. OCI-based VLC system. (a) 4 × 5 LED array transmitter. (b) Camera receiver.

Fig. 11. Experimental setup, LED transmitter, and OCI-based camera receiver.

TABLE 2

LED transmitter specifications

Peak emission wavelength	630 nm (red)
Measured cut-off frequency	14.5 MHz
Half intensity angle	8°
Forward voltage range, V_{p-p}	0.72 V

active, as is the case in practical use. The signal waveform received is first amplified and then stored digitally in the oscilloscope after low-pass filtering. The decoding process is done offline.

Note that the communication performance of the image-sensor-based VLC system is independent of communication distance [9]. Additionally, The OCI-based camera receiver has demonstrated accurate and quick LED detection under outdoor mobile environments. Thus, although the experiments involve a short distance and fixed conditions, the results are expected to apply to actual outdoor mobile environments.

Tables 2 and 3 list the specifications of the LED transmitter and the settings of the camera receiver.

4.2. Parameters of Optical-OFDM

The parameters of the optical-OFDM and FEC coding are listed in Tables 4 and 5, respectively. The number of FFT points is 128 and the CP length is 8. The number N of all subcarriers is set to 106. However, the number of subcarriers that can be modulated by unique data symbols decreases to 52 because of the Hermitian symmetry structure and unmodulated DC subcarriers. The number of data symbols and training symbols in a frame are 4 and 24, respectively. The number of data subcarrier is 52 and the interval of training symbols that

TABLE 3

Camera receiver settings

Lens focal length	50 mm
Cut-off frequency of LPF	35 MHz
Tx–Rx distance	1.5 m

TABLE 4

Optical-OFDM model parameters

Number of FFT point	128
Number of unique data subcarriers	52
Subcarrier modulation scheme	BPSK, 4-QAM, 8-QAM, ..., 256-QAM
Number of cyclic prefix	8
Number of training symbols (1 frame)	4
Number of data symbols (1 frame)	24
Proportionally constant μ	3
Signal bandwidth	32 MHz
Subcarrier interval	610.0 kHz
Frame interval	49.54 μs
Target throughput	45, 50, 55 Mbps

equals the interval of four OFDM symbols is set to be compliant with the IEEE 802.11p DSRC standard.

The signal bandwidth is set to about 32 MHz and the subcarrier interval is set to almost 610.0 kHz. According to the added CP length, the length of the each OFDM symbol is $(128 + 8)/(128 \times 610.0 \text{ kHz}) \cong 1.742 \ \mu s$, and therefore, the interval between all OFDM symbols per frame is $(24 + 4) \times 1.742 \cong 48.74 \ \mu s$. The time between two successive frames is set to 0.8 μs, and therefore, the resulting the frame interval is $48.74 + 0.8 = 49.54 \ \mu s$.

The modulation schemes (constellation orders) of each subcarrier are determined based on the target number of bits per OFDM symbol, as discussed in the previous section. Note that this number depends on the target throughput, convolutional coding rate, and frame interval. If the target throughput is 55 Mbps with a convolutional code rate of 1/2, the required bit rate is 110 Mbps and the required number of bits per frame is 110 Mbps $\times$ 49.54 μs = 5449.4 bits. In this case, the number of bits per OFDM symbol must be at least 5449.4/24 $\cong$ 227.1 bits. Because the number of bits must be an integer, 228 bits are required. According to the required number of bits, the subcarrier modulation schemes are determined based on the bit-loading algorithm.

4.3. BER Measurement Results

Table 6 shows the results of BER measurements. For 45 Mbps with code rates 3/4 and 1/2, the results are error free. For 50 and 55 Mbps, a BER of 10^{-6} order is obtained.

In [20], the required communication performance for automotive applications is BER $< 10^{-5}$. In this case, the data rate of 55 Mbps per pixel is practical for OCI-based VLC systems and the system exceeds the currently available V2I and V2I communication standards [20]–[22] in terms of data rates. We emphasize that the communication performance of the OCI-based VLC system is stable as communication distance increases and under movement of the LED transmitter and/or the OCI-based receiver. Thus, we expected to obtain a 55 Mbps data rate in actual outdoor mobile environments.

TABLE 5

FEC coding parameters

Coding scheme	Convolutional code
Constraint length	7
Coding rate	3/4, 1/2
Decoding scheme	Soft decision Viterbi decoding (8-bit quantized)

TABLE 6

BER measurement results

Coding rate	Target bit rate [Mbps]	Throughput [Mbps]	BER	
3/4	60	45	0	$(0/1.01 \times 10^7)$
	66.7	50	7.86×10^{-7}	$(8/1.02 \times 10^7)$
	73.3	55	4.48×10^{-6}	$(49/1.09 \times 10^7)$
1/2	90	45	0	$(0/1.01 \times 10^7)$
	100	50	3.11×10^{-6}	$(32/1.03 \times 10^7)$
	110	55	9.17×10^{-6}	$(99/1.08 \times 10^7)$

As shown in Fig. 10(a), we use 4×5 LED array transmitter, and each LED transmits the same optical-OFDM signal. Therefore, we may expect that at least one LED can be clearly seen at the image sensor even on a rough road. In other words, if the light source is within field-of-view (FOV), then it is possible to receive signal. However, as the extreme case of a very bumpy road that the light source goes out of FOV, the image sensor receiver can not resolve the VLC signal.

5. Conclusion

In this paper, we proposed a new automotive VLC system based on the OCI and that applies DCO-OFDM to achieve more flexible and effective signal transmission. For higher data rates, we consider the characteristics of the LED and OCI to select the appropriate parameter values for signal processing.

First, we investigated the forward current of the LED. Although increasing the range of the LED forward current to the extent possible is desirable to ensure a high SNR, the range is restricted by practical considerations. Based on the specifications of the LEDs, the minimum and maximum tolerable currents are determined. In addition, the average forward current is set to the rated current so that the LED may serve its primary role, as a light source.

Next, we selected the parameter values such as the proportionality constant μ and signal bandwidth based on the channel capacity, which we calculated from the estimated SNRs of each subcarrier. If μ is too small, clipping the waveform significantly degrades the capacity. In contrast, an excessively large μ lowers the amplitude of optical signals with respect to the forward-voltage range of the LED; this causes the decay of the SNR of each subcarrier or, equivalently, the total capacity. Furthermore, increasing the bandwidth is effective for increasing the capacity; however, the high-frequency attenuation of the OCI limits the available bandwidth. The estimation of the SNR and capacity calculation should target $\mu = 3$ and a signal bandwidth of approximately 30 MHz.

Finally, we applied bit-loading for DCO-OFDM. Bit loading allocates data so that the throughput of each subcarrier is maximized to suit the channel characteristics. The bit-loading algorithm is applied that allocates bits into the subcarriers to minimize the average BER and guarantees the target bit rate.

The data-transmission experiment demonstrated that the OCI-based DCO-OFDM system achieves a data rate of 45 Mbps without bit errors and 55 Mbps with a BER $< 10^{-5}$. This result is five-fold greater than that obtained with our previous system; the proposed system exceeds the automotive communication standards based on radio frequencies, such as the IEEE 802.11p standard, in terms of the data rates.

Acknowledgment

References

[1] J. Boyd, "Japan's plan to speed self-driving cars," *IEEE Spectrum*, Nov. 17 2015, [Online]. Available: http://spectrum. ieee.org/cars-that-think/transportation/self-driving/japans-plan-to-speed-selfdriving-cars

[2] T. Luettel, M. Himmelsbach, and H. J. Wuensche, "Autonomous ground vehicles—Concepts and a path to the future," *Proc. IEEE*, vol. 100, Special Centennial Issue, pp. 1831–1839, May 2012.

[3] M. R. Hafner, D. Cunningham, L. Caminiti, and D. Del Vecchio, "Cooperative collision avoidance at intersections: Algorithms and experiments," *IEEE Trans. Intell. Transp. Syst.*, vol. 14, no. 3, pp. 1162–1175, Sep. 2013.

[4] A. Joshi and M. R. James, "Generation of accurate lane-level maps from coarse prior maps and LIDAR," *IEEE Intell. Transp. Syst. Mag.*, vol. 7, no. 1, pp. 19–29, Spring 2015.

[5] R. O. Chavez-Garcia and O. Aycard, "Multiple sensor fusion and classification for moving object detection and tracking," *IEEE Trans. Intell. Transp. Syst.*, vol. 17, no. 2, pp. 525–534, Feb. 2016.

[6] J. Fritsch, T. Kühnl, and F. Kummert, "Monocular road terrain detection by combining visual and spatial information," *IEEE Trans. Intell. Transp. Syst.*, vol. 15, no. 4, pp. 1586–1596, Aug. 2014.

[7] A. Cord and N. Gimonet, "Detecting unfocused raindrops: In-vehicle multipurpose cameras," *IEEE Robot. Autom. Mag.*, vol. 21, no. 1, pp. 49–56, Mar. 2014.

[8] T. Yamazato *et al.*, "Image-sensor-based visible light communication for automotive applications," *IEEE Commun. Mag.*, vol. 52, no. 7, pp. 88–97, Jul. 2014.

[9] T. Yamazato *et al.*, "Vehicle motion and pixel illumination modeling for image sensor based visible light communication," *IEEE J. Sel. Areas Commun.*, vol. 33, no. 9, pp. 1793–1805, Sep. 2015.

[10] N. Iizuka, "Image sensor communication: A new way of visible light communication," in *Proc. Int. Display Workshop*, 2010, pp. 2193–2196.

[11] T. Saito, S. Haruyama, and M. Nakagawa, "A new tracking method using image sensor and photo diode for visible light road-to-vehicle communication," in *Proc. IEEE 10th ICACT*, Feb. 2008, vol. 1, pp. 673–678.

[12] S. Nishimoto *et al.*, "High-speed transmission of overlay coding for road-to-vehicle visible light communication using LED array and high-speed camera," in *Proc. IEEE OWC*, Dec. 2012, pp. 1234–1238.

[13] K. Ebihara, K. Kamakura, and T. Yamazato, "Layered transmission of space–time coded signals for image-sensor-based visible light communications," *J. Lightw. Technol.*, vol. 33, no. 20, pp. 4193–4206, Oct. 2015.

[14] T. Yamazato and S. Haruyama, "Image sensor based visible light communication and its application to pose, position, and range estimations," *IEICE Trans. Commun.*, vol. E97-B, no. 9, pp. 1759–1765, Sep. 2014.

[15] N. Matsushita *et al.*, "Id cam: A smart camera for scene capturing and id recognition," in *Proc. 2nd IEEE/ACM Int. Symp. Mixed Augmented Reality*, Oct. 2003, pp. 227–236.

[16] I. Takai *et al.*, "LED and CMOS image sensor based optical wireless communication system for automotive applications," *IEEE Photon. J.*, vol. 5, no. 5, Oct. 2013, Art. no. 6801418.

[17] I. Takai *et al.*, "Optical vehicle-to-vehicle communication system using LED transmitter and camera receiver," *IEEE Photon. J.*, vol. 6, no. 5, Oct. 2014, Art. no. 7902513.

[18] R. Mesleh, H. Elgala, and H. Haas, "On the performance of different OFDM based optical wireless communication systems," *IEEE/OSA J. Opt. Commun. Netw.*, vol. 3, no. 8, pp. 620–628, Aug. 2011.

[19] L. Gavrilovska, S. Krco, V. Milutinovic, I. Stojmenovic, and R. Trobec, "Application and multidisciplinary aspects of wireless sensor networks," *Comput. Commun. Netw.*, 2011.

[20] "700 MHz band intelligent transport systems ARIB STD-T109, Assoc. Radio Ind. Bus., Chiyoda-ku, Tokyo, Japan, 2012. [Online]. Available: http://www.arib.or.jp/english/html/overview/doc/5-STD-T109v1_2-E1.pdf

[21] "Dedicated short-range communication system ARIB STD-T75, Assoc. Radio Ind. Bus., Chiyoda-ku, Tokyo, Japan, 2003. [Online]. Available: http://www.arib.or.jp/english/html/overview/doc/5-STD-T75v1_0-E2.pdf

[22] A. M. S. Abdelgader and W. Lenan, "The physical layer of the IEEE 802.11p WAVE communication standard: The specifications and challenges," in *Proc. WCECS*, pp. 691–698, Oct. 2014.

[23] J. Armstrong, "OFDM for optical communications," *J. Lightw. Technol.*, vol. 27, no. 3, pp. 189–204, Feb. 2009.

[24] S. Dimitrov and H. Haas, "Information rate of OFDM-based optical wireless communication systems with nonlinear distortion," *J. Lightw. Technol.*, vol. 31, no. 6, pp. 918–929, Mar. 2013.

[25] S. D. Dissanayake and J. Armstrong, "Comparison of ACO-OFDM, DCO-OFDM and ADO-OFDM in IM/DD systems," *J. Lightw. Technol.*, vol. 31, no. 7, pp. 1063–1072, Apr. 2013.

[26] S. Dimitrov, S. Sinanovic, and H. Haas, "Clipping noise in ofdm-based optical wireless communication systems," *IEEE Trans. Commun.*, vol. 60, no. 4, pp. 1072–1081, Apr. 2012.

[27] N. Chi, M. Zhang, Y. Wang, and X. Lu, "Experimental demonstration of high-speed WDM VLC systems employing high-order CAP modulation," in *Proc. ICEVLC*, Oct. 2015, pp. 1–5.

[28] R. A. Shafik, M. S. Rahman, and A. R. Islam, "On the extended relationships among EVM, BER and SNR as performance metrics," in *Proc. IEEE Int. Conf. Electr. Comput. Eng.*, Dec. 2006, pp. 408–411.

[29] H. Ko, S. Oh, B. Kim, and C. Kim, "Simple bit allocation algorithms with BER-constraint for OFDM-based systems," in *Proc. IEEE Wireless Commun. Netw. Conf.*, Apr. 2009, pp. 1–5.

[30] C. Assimakopoulos and F.-N. Pavlidou, "New bit loading algorithms for DMT systems based," in *Proc. IEEE Global Telecommun. Conf.*, Mar. 1996, pp. 724–728.

[31] K. Cho and D. Yoon, "On the general BER expression of one- and two-dimensional amplitude modulations," *IEEE Trans. Commun.*, vol. 50, no. 7, pp. 1074–1080, Jul. 2002.